Friction Stir Welding of Extruded Powder Metallurgy Al Alloy

Friction stir welding was used successfully to join an extruded powder metallurgy Al alloy without discontinuities, voids, or defects

BY A. ELREFAEY, K. ANDERS, H. KILIAN, F. ELLERMANN, AND W. KÜHLEIN

ABSTRACT

Friction stir welding (FSW) of an extruded powder metallurgy (PM) aluminum alloy was performed to produce a rotary engine housing. The microstructure, phase constituents, and mechanical properties of FSW joints were studied by metallography, tensile, and fatigue tests. The results indicated the process achieved sound joints without voids or discontinuities. The microstructure of welded area (stir zone) was finer and more homogeneous than the base metal, while the average yield strength value was 2.3% higher than the base metal. Meanwhile, the average tensile strength was 95% that of the base metal. Furthermore, statistical evaluation at 10, 50, and 90% probabilities of survival of the fatigue test stresses were calculated as 81.94, 81.01, and 80.09 MPa, respectively, at room temperature. Meanwhile, the fatigue limit decreased approximately 25% due to raising the temperature to 240°C.

KEYWORDS

• Friction Stir Welding (FSW) • Aluminum • Microstructure • Tension
• Fatigue • Powder Metallurgy (PM)

Introduction

As the automotive industry addresses environmental concerns, the problems of fuel consumption and weight reduction have come to the fore. Reducing the weight of automobiles is one of the primary means by which their fuel consumption is lowered. In addition to saving fuel, weight reduction is a very effective way to improve the car's driving and drifting abilities. It improves just about everything a car has to offer: acceleration, braking, handling, and CO_2 emission.

To comply with all of the previously mentioned changes, automotive manufacturers worldwide are exploring alternative lightweight materials such as aluminum.

Aluminum alloys are not only lightweight materials, but they also have excellent corrosion resistance, high workability, good thermal conductivity, and highly recyclable properties. For these reasons, aluminum is expected to replace many parts in the automotive industry. The processing and manufacturing process plays a vital role in the final properties of alu-

minum and aluminum alloys. For example, liquid phase processes such as conventional casting are cost effective but cannot be used to make components for critical applications since low mechanical property levels can be obtained as a result of coarser microstructural features commonly associated with conventionally cast materials. Alloys produced by atomization followed by powder metallurgy (PM) consolidation and extrusion to the final shape overcome the formation of coarse grains, coarse constituents, and macrosegregation because of the high cooling rates. Therefore, these PM alloys are characterized by very fine, homogeneous, and segregation-free microstructures combined with a fine distribution of intermetallic particles. Powder metallurgy alloys are now a potential alloy for the Wankel rotary engine housing and the single rotary piston to reduce weight of these components compared with the heavier conventional quench and tempered steel. Reducing the weight of these components would, in turn, reduce the amount of necessary counterweight, and therefore reduce acceleration losses (Refs. 1, 2).

The PM alloys help to realize superior properties but have limitations related to the dimensions of the component and, in addition, involve high costs (Refs. 3–7). As the component size increases, the extrusion process becomes difficult to perform, the power needed is proportionally increased,

A. ELREFAEY (ahmed.elrefaei@ait.ac.at), K. ANDERS, and H. KILIAN are with Mobility Dept., LKR Leichtmetallkompetenzzentrum, Ranshofen GmbH (Light Metals Technologies Ranshofen), Austrian Institute of Technology, Ranshofen, Austria. F. ELLERMANN and W. KÜHLEIN are with Hammerer Aluminium Industries Extrusion GmbH, Ranshofen, Austria.
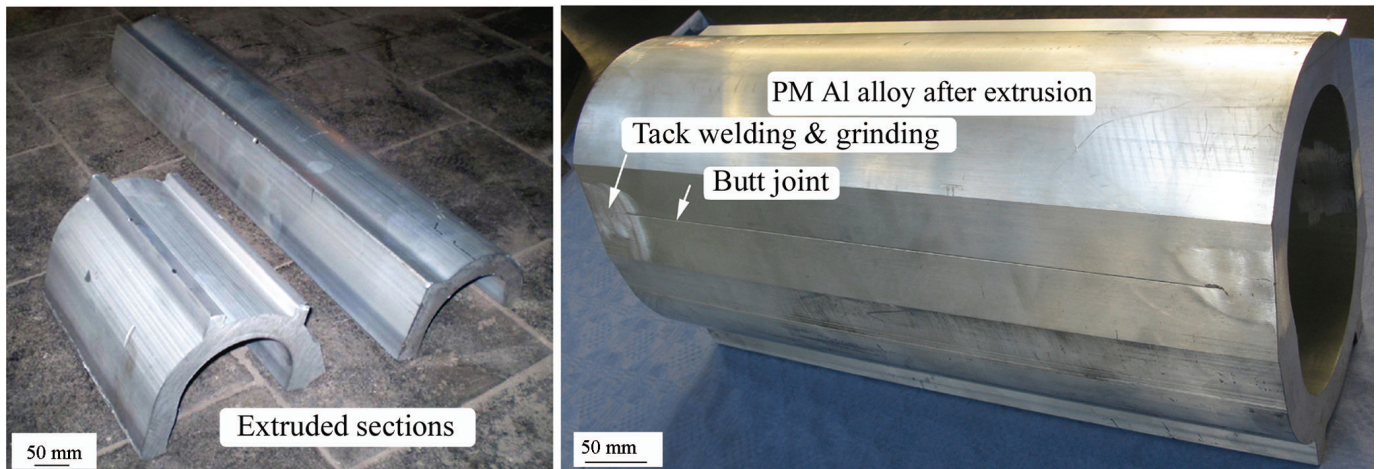
Fig. 1 — Samples of extruded sections and the joint configuration before welding.
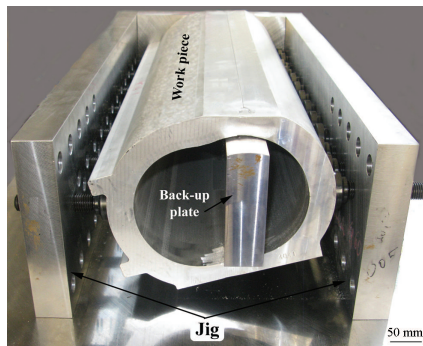

Fig. 2 — The workpiece clamped in the jig before FSW.

and the cost becomes unaffordable. Therefore, a need for a joining process to assemble different extruded parts is necessary.

Friction stir welding has the potential to join PM Al alloys since it has been systematically developed for joining aluminum alloys. It is proving to be far more forgiving to use than arc welding techniques and can consistently produce long welds, especially between extrusions of high quality, low cost, and with very low distortion since the weld is made in the solid phase (Refs. 8, 9). Additionally, PM processed aluminum alloys suffer from three major microstructural problems that limit their full potential: prior-particle boundaries with an aluminum oxide film, microstructural inhomogeneity, and remnant porosity. These microstructural features particularly hamper the ductility in very high-strength aluminum alloys and impede the welding process as well. Therefore, in addition to the need for a welding process to join the materi-

al, a microstructure homogenization process is also required. The unique advantages of FSW, in respect to welding and microstructure homogenization, can easily overcome the limitations of welded PM aluminum alloys and enhances their mechanical properties (Refs. 8, 10–13).

In recent years, several studies have been concentrated on friction stir processing of aluminum alloys, PM alloys, and composites to homogenize and refine the microstructure (Refs. 13–16). However, as far as we know, little or no studies have been reported on PM aluminum alloys after final forming by the extrusion process. In this study, a eutectic PM Al-Si alloy after extrusion has been welded by the FSW process. Therefore, this research has been aimed at investigating the microstructural features, phase analysis, and mechanical properties of the joints.

Experimental Work

Material

The starting material was an air-atomized powder aluminum alloy sieved to <150 μm (Mepura Metallpulvergesellschaft m.b.H, Austria) with a density of 2.775 g/cm^3. Consolidation was done by cold compaction using an external pressure of 200 MPa. The bulk material, having 300 mm diameter and 750 mm length, was hot extruded into two half sections with a reduction ratio of 9:1 after holding for 12 h at 450°C. None of the extruded bars showed blistering or cracking on the surface. The chemical analysis of the alloy after extrusion is

given in Table 1. Two 20-mm-thick extruded sections were assembled by tack welding before FSW to produce the rotary engine housing. Figure 1 shows a sample of the extruded sections and the configuration of the joint before welding.

FSW Process

The workpiece was placed on a backup plate and the whole geometry was rigidly clamped with a jig to prevent lateral movements during FSW. Figure 2 shows the workpiece clamped in the jig before the FSW process.

A welding tool having a 16-mm pin diameter made from tool steel was used. The tool axis was tilted by 2 deg with respect to the vertical axis of the plate surface. The applied rotation speed was 500 rev/min, with a traveling speed of 200 mm/min, and a compressive force of 35 kN. The FSW tool, fixed in the holder, was slowly pushed into the PM Al plate and then forcibly traversed along the joint until the end of the weld was reached. The welding tool was then retracted while the tool continued to turn.

Microstructure and Mechanical Testing

The cross sections of the joints were prepared for metallographic analysis with standard grinding and polishing techniques. Selected samples were subsequently etched for 30 s with a solution comprised of 50% water, 15% HCl, 25% HNO$_3$, and 10% HF. The microstructure of the joints was

examined with a light optical microscope and grain size measurements were performed with digital image analysis software. A scanning electron microscope (SEM), equipped with an energy-dispersive X-ray (EDX), was used for chemical analysis.

For the tensile tests, 140-mm-long flat samples and 115-mm-long round samples were prepared in accordance with DIN 50125 at room temperature (Ref. 17). The weld was centered in the gauge section and the loading axis, normal to the welding direction, was applied. Sixteen round and flat samples were used to calculate the average yield strength, tensile strength, and ductility of the joints. Tensile strength was determined by dividing the maximum load required during testing by the cross-sectional area. It is worth noting that transverse weld specimens normally provide a measure of joint efficiency in terms of strength, but do not provide a good ductility measurement of the weld.

Since engineered parts are frequently subjected to stress by dynamic forces, especially alternating or cyclic loads, which act periodically in the same manner on the structural part, it is necessary to evaluate the behavior of a material under such loads by fatigue tests up to very high load-cycle rates. The results are presented in what are known as Wöhler diagrams or an S-N curve obtained by plotting the applied stress (S) against the number of cycles to failure (N). The fatigue strength or endurance limit is defined as the stress level a sample can withstand for at least 10^7 cycles.

The high cycle fatigue specimens were tested using a sinusoidal wave form in accordance with DIN 50100 (Ref. 18) in air at room temperature and 240°C on a RUMUL AG Testronic 100-kN tester. A test frequency between 70 and 90 Hz and a load ratio of –1 were used. The stress concentration factor is equal to 1, and the tests were terminated at 10^7 cycles. Fatigue tests were comparatively and statistically evaluated according to the arcsin √p-method (Ref. 19). Using this method, the fracture probabilities of 10, 50, and 90% were estimated. The fatigue crack initiation site and crack propagation mechanisms were examined on the fracture surfaces of failed samples via SEM. Hardness measurement was performed with the help of a Vickers hardness testing ma-
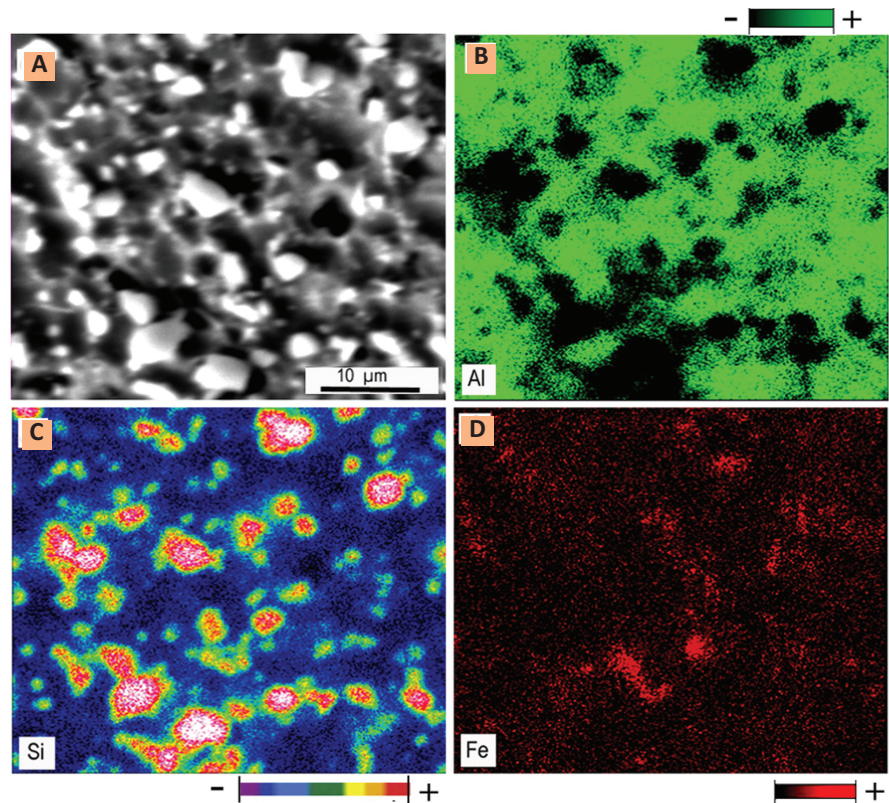

Fig. 3 — A — Microstructure of the extruded alloy; EDX mapping of, respectively, B — Al; C — Si; D — Fe.

chine at 0.1-kgf loads and an indentation time of 25 s.

Results and Discussion

Microstructure of Joints

The microstructure of the extruded alloy is shown in Fig. 3A. The PM Al-Si alloys presented a fragmented eutectic (α-aluminum + silicon) microstructure. Owing to the processing history of the alloy, the microstructure is composed of very fine silicon particles scattered in the α-Al matrix. The presence of these phases is in accordance with the equilibrium microstructural phases predicted by the binary Al-Si phase diagram (Ref. 20). The average Si size in the extruded section is 2.9 μm. This structure is necessary to achieve good mechanical performance of the consolidated material. Furthermore, the Al-Si alloy has some other coexisting elements such as iron, copper, magnesium, manganese, and zinc. The solubility of these elements in aluminum usually increases with increasing temperature. At room tempera-

ture, these elements usually constitute precipitation of Si, Mn, and Fe, and forms an $Al_{12}(Fe,Mn)_3Si$ phase. The wide variety of intermetallic phases in aluminum alloys occurs because aluminum is highly electronegative and trivalent, which has been the subject of several studies (Refs. 21–23). Therefore, very fine precipitation was scattered in the aluminum matrix. Figure 3B–D shows EDX mapping of Al, Si, and Fe, respectively, in the Al alloy. It is obvious that aluminum constituted the matrix and disappeared at the presence of Si particles. Owing to the low Si measuring sensitivity in the case of very fine particles, concentration of silicon seemed depleted (see fine green area at the microstructure, Fig. 3C) at the regions where fine particles were formed. Iron was detected with less concentration at random places throughout the microstructure, as shown in Fig. 3D.

The macrostructure of the joint after FSW is shown in Fig. 4A. The flash is only released on the retreating side, where the direction of the tool rotation moves in the opposite direction to
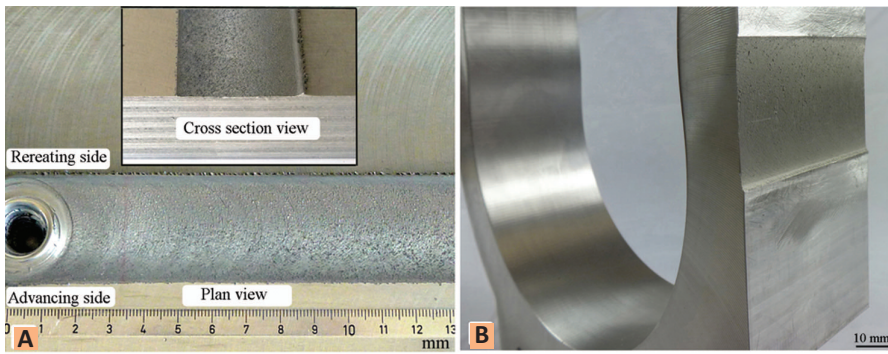
Fig. 4 — A — Macrostructure of the joint after FSW; B — geometry of rotary engine housing after grinding and cleaning.
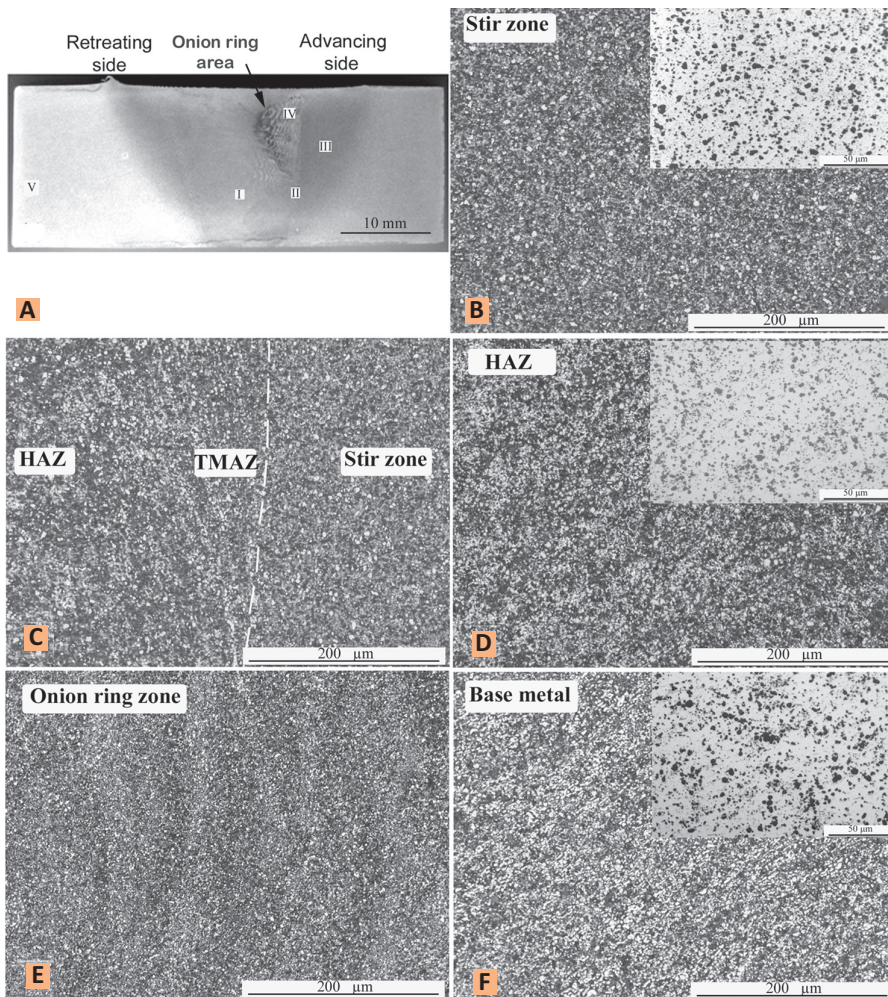

Fig. 5 — Characteristic microstructure of the joint: A — Cross-section macrostructure; B — microstructure of the stir zone I; C — microstructure at the stir zone/HAZ interface II; D — microstructure of the HAZ III; E — microstructure of the onion ring zone IV; F — microstructure of base metal V.

area of the weld, close to the advancing side. Previous studies reported the presence of this onion ring in the whole weld nugget and clear thermomechanically affected zone (TMAZ) at both sides of the joint on FSW of aluminum alloys (Refs. 24–26).

The microstructure of the joint stir zone (area I in Fig. 5A) was characterized by the silicon particles in the α-Al matrix — Fig. 5B. As clearly shown from the microstructure without etching at the top right of Fig. 5A, F, the structure of the stir zone is finer and more homogeneous than the structure of the base metal. The Si particles showed an average grain size of 2.1 µm, which is approximately 28% finer than the base metal. This is partially due to the amount of plastic strain caused by the FSW pin and shoulder, which leads to more disruption of the silicon and consequently smaller grain size (Refs. 27–30). There was a very smooth transition area in between the stir zone and the adjacent regions at both sides of the joints. Figure 5C shows this area at the advancing side, which is hard to detect; therefore, a dashed white line was drawn to distinguish this area. A TMAZ with a slightly deformed structure was observed beside this area at both sides of the joints. Furthermore, adjacent to the TMAZ, a HAZ characterized by a microstructure similar to the base metal was formed, as shown in Fig. 5D.

As mentioned previously, an onion ring pattern was observed at the top area of the weld close to the advancing side. Figure 5E shows the microstructure of this zone. It is generally known that the onion ring pattern results from the interaction between the material flow driven by the rotating pin and the shoulder-driven flow. This interaction is observed by the deformation of the onion rings in the advancing side of the weld. Several studies have focused on the formation of these patterns. However, detailed explanations and discussions of this phenomenon is out of the scope of the present study. Furthermore, there has been no reported correlation between the phenomenon and the resulting quality of the weld nugget (Ref. 8).

Figure 6 shows SEM micrographs of the base metal (A) and the stir zone (B). In addition to the finer and more homogeneous distribution of silicon in the stir zone, fragmented particles of

the travel direction. The geometry of the rotary engine housing after grinding and cleaning is shown in Fig. 4B.

Macrostructures of the traverse sections of the joints are shown in Fig.

5A. It is worth noting that there are no pores or unbounded areas, and a sound weld was achieved. One of the main joint features is the observed small onion ring structure at the top

eutectic were crushed in the matrix of the stir zone as clearly shown by arrows at the top right of Fig. 6B. There was almost no difference in chemical compositions between the components of microstructure of stir zone and base metal.

Mechanical Properties

The mechanical properties of the FSW joints and the base metal are given in Table 2. Surprisingly, the offset yield point ($R_{p0.2}$) of welded joints is 2.3% higher than the base metal. Meanwhile, the average maximum tensile strength of the welded joints is 95% that of the base metal. The reason for the improved mechanical properties of the welded joints is the severe plastic deformation offered by the FSW process in addition to the grain size refinement in the weld metal area. These strengthening mechanisms hinder dislocation motion and render the material stronger than it was previously (Refs. 31, 32). The reduction in area of the welded joints was almost half of the values reported for the base metal, and all welded samples showed failure outside the welded region, which is an indication of defect-free joints. Figure 7 shows a tension sample after testing in addition to a fatigue test sample that will be discussed later. Further investigations were performed by analyzing the fracture surface of the samples. Figure 8A shows a general view of the tensile fracture surface whose fracture featured a lot of tears, ridges, and a few cracks at different areas. The rough topography is due to the macroscopic fracture process occurring on a plane that is at some angles to the applied stress direction in the tensile specimen. A closer observation of the rectangular area in Fig. 8A is shown in Fig. 8B. A dimple-like structure is prominent in the morphology. However, some Si particles and voids originated by the unattached silicon were clearly observed in the second close-up view in Fig. 8C. The Si particles, confirmed by EDX analyses, and corresponding voids are indicated by black and light arrows, respectively. The presence of these areas close to the crack is an indication of the initiation of the crack owing to the Si particles. It is reported that damage and failure of Al-Si alloys is generally associated with initiation and growth of cracks in the Si particles (Refs. 27, 33).
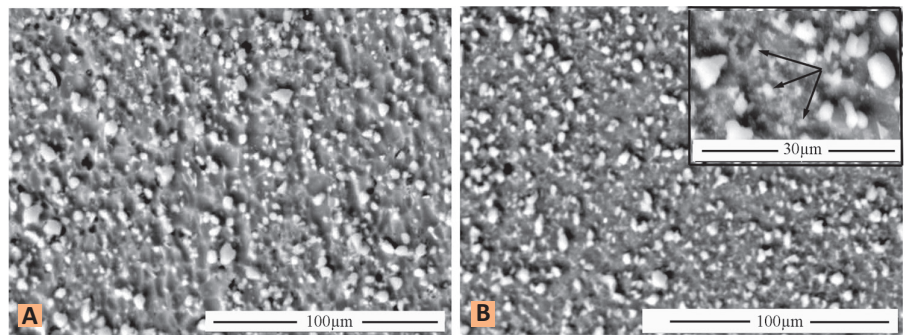

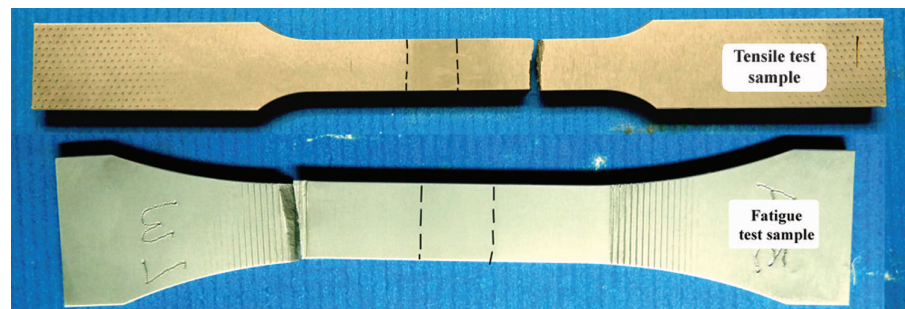Fig. 6 — SEM micrographs of the following: A — Base metal; B — stir zone.

Fig. 7 — Macrograph of fractured samples in tensile and fatigue tests.
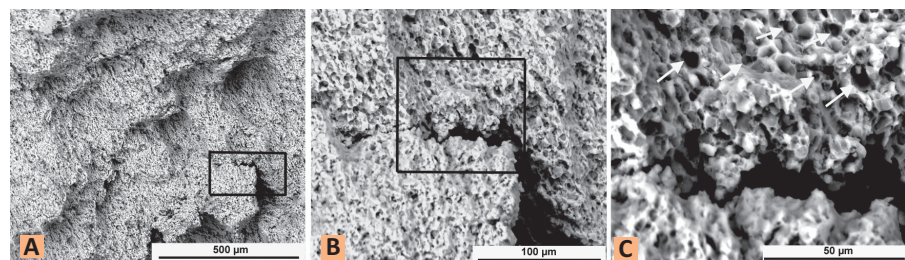

Fig. 8 — SEM of fracture tension sample: A — General view of the surface; B — magnified view of the propagated crack; C — dimple-like fracture surface.

Statistical evaluation of the fatigue test stresses for 10, 50, and 90% probabilities of survival was estimated at room temperature and also at 240°C. Figure 9 shows the plotted SN curves. The obtained data for the fatigue limit are listed in the graph. Fatigue test stresses at room temperature for 10, 50 and 90% probabilities of survival were calculated as 81.94, 81.01, and 80.09 MPa, respectively. All samples were fractured outside the joined area as shown in Fig 7. The fatigue limit decreased approximately 25% due to raising the temperature to 240°C. Additionally, the base metal fatigue test stresses at room temperature for 10, 50, and 90% probabilities of survival were 82.32, 81.27, and 79.92 MPa, respectively. It is also noted that (not included in Fig. 9) the fatigue characteristics of welded sam-

ples, at room temperature, are quite similar to base metals, which is an indication of sound welded joints.

Figure 10A shows the postfatigued fracture surface of sample failed after 877706 cycles under a stress of 81.25 MPa and at room temperature. Crack initiation sites were at or near the surface as shown by arrows in Fig. 10A, D. Since the silicon particles are stiffer than the matrix, the stress concentration created in this area is enough to cause microslips in the matrix close to the silicon particles, which leads to the particle debonding and then crack initiation (Ref. 34). Under a condition of relatively high stress levels, especially in aluminum alloys, quite large numbers of microcracks were formed (Refs. 33, 35). At a later stage, linking up of these cracks occurred to form one sin-
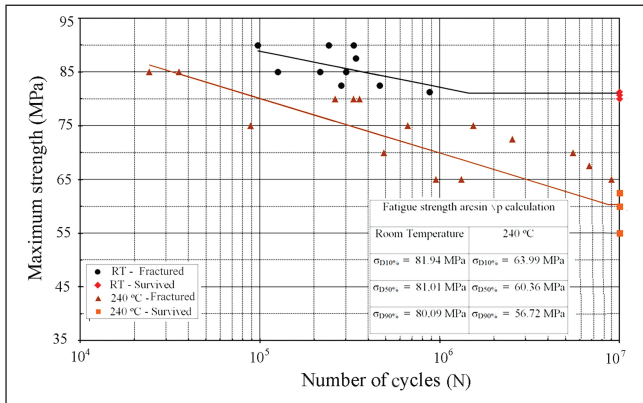
Fig. 9 — SN curves for the fatigue samples at room temperature and 240°C.

Fig. 10 — Postfatigued fracture surface: A — Overview of the fracture surface of sample tested at room temperature; B — magnified view of one of the crack-initiation areas and the propagation direction at room temperature; C — magnified view of the flat and tear areas at room temperature; D — overview of the fracture surface of the sample tested at 240°C; E — magnified view of one of the crack-initiation areas and the propagation direction tested at 240°C; F — magnified view of the tear area tested at 240°C.
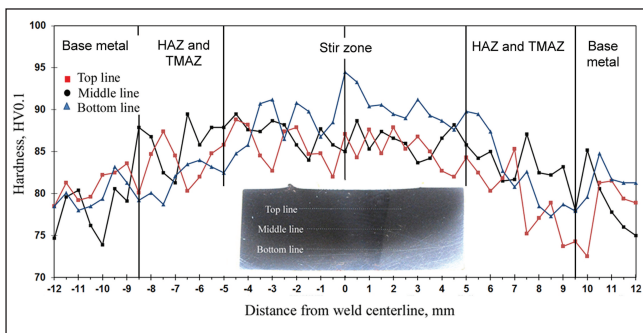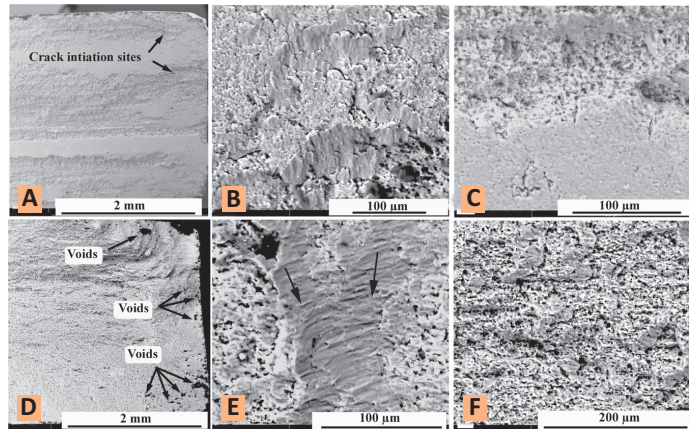

Fig. 11 — Microhardness distributions at the top, middle, and bottom of the FSW joint.

gle larger crack. A flat fracture surface is observed at some parts; meanwhile, the main fracture area was fairly ductile. Figure 10B shows a magnified view of one of the crack-initiation areas and the propagation direction. Meanwhile, Fig. 10C shows both flat and tear areas at high magnification. It is also worth noting that striation features were not detected at the fracture surface probably because of the very fine microstructure.

At high temperature, voids were observed at the sample edges that are believed to be the origin of the crack initiation. The formation mechanism of these voids is not clear but it could be the result of interactions of very small silicon particles, which act as micronotches with cyclic stress. Figure 10D shows these voids at the edges of the fracture surface area, which initiated the cracks. The crack propagation direction at high magnification is clearly observed in Fig. 10E, meanwhile, the rest of the fracture surface is composed of the dimple-like structure and tear areas as shown in Fig. 10F.

The microhardness distributions across the welded joint including the base metal, HAZ, TMAZ, and stir zone are shown in Fig. 11. The difference in hardness values at the top, middle, and bottom of the joint is very small. The HAZ and TMAZ areas at both the advancing and retreating sides of the joints were found to have the minimum hardness compared to the other regions of the weld. Probably this is caused by the annealing effect during processing (Refs. 36, 37). Also, the highest hardness values were achieved in the stir zone because of the fine grain size and the severe plastic deformation at these areas (Refs. 37, 38). The average hardness value of stir zone, HAZ, and base metal were 89, 74, and 79 HV0.1, respectively.

Conclusions

A 20-mm-thick PM aluminum alloy has been welded by FSW to produce a rotary engine housing after the extrusion process. Detailed characteristic microstructure and mechanical investigation were evaluated. The following conclusions were reached:

1) FSW was successfully used to join the extruded PM Al alloy without discontinuities, voids, or defects. Compared to the base metal microstructure, fine and more homogeneously distributed structures were detected after joining. The microstructure of the welded joint at all regions was composed of very fine silicon particles scattered in the α-Al matrix.

2) The achieved yield point of the welded joints is 2.3% higher than the base metal, while the maximum tensile strength is 95% that of the base metal. Additionally, the fatigue limit decreased approximately 25% due to raising the temperature from room temperature to 240°C. Fracture of joints after tensile and fatigue tests was always in the base metal.

3) Failure of Al-Si alloys was associated with initiation and growth of cracks at the Si particles. The morphology of the fracture was mainly ductile after tension and fatigue tests.

4) The maximum hardness of the joint was observed in the stir zone because of its fine grain size. Meanwhile, the HAZ and TMAZ areas achieved the lowest hardness level in the joint.

References

1. Atzwanger, M., Hubmann, C., Kometter, B., Friedl, H., and Schöffmann, W. 2010. Two cylinder gasoline engine concept for highly integrated range extender and hybrid powertrain applications. *SAE Technical Paper 2010-32-0130*, doi:10.4271/2010-32-0130.

2. Chimani, C. M., and Uggowitzer, P. J. 2012. Innovative preparation methods for components of a range extender rotary engine. Tagungsband, 7. *Ranshofener Leichtmetalltage*, pp. 172–184, Austurian Institute of Technology, Munderfing.

3. Van Vlack, L. H. 1989. *Elements of Materials Science and Engineering*. 6th ed. pp. 418–421. Prentice Hall, USA.

4. Davis, J. R. 1993. *ASM Specialty Handbook: Aluminum and Aluminum Alloys*. pp. 143–159, Materials Park, Ohio: ASM International.

5. Neubing, H. C. 1981. Production and properties of aluminum powder for powder metallurgy. *Powder Metallurgy International* 3: 74–78.

6. Salaci, E. 2002. Mechanical properties of spray cast 7XXX series aluminium alloys. *Turkish Journal of Engineering and Environmental Sciences* 26: 345–352.

7. Hanlon, T., Kwon, Y. N., and Suresh, S. 2003. Grain size effects on the fatigue response of nanocrystalline metals. *Scripta Materialia* 49: 675–690.

8. Mishra, S. R., and Mahoney, M. W. 2007. *Friction Stir Welding and Processing*. pp. 1–6. Materials Park, Ohio: ASM International.

9. Elrefaey, A., Gouda, M., Takahashi, M., and Ikeuchi, K. 2005. Characterization of aluminum/steel lap joint by friction stir welding. *Journal of Materials Engineering and Performance* 14: 1–9.

10. Berbon, P. B., Bingel, W. H., Mishra, R. S., Bampton, C. C., and Mahoney, M. W. 2001. Friction stir processing: A tool to homogenize nanocomposite aluminum alloys. *Scripta Materialia* 44: 61–66.

11. Jata, K. V. 2001. *Friction Stir Welding and Processing*. Warrendale, Pa.: TMS - The Minerals, Metals & Materials Society, pp. 235–242.

12. Jata, K.V. 2003. *Friction Stir Welding and Processing II*. Warrendale, Pa.: TMS - The Minerals, Metals & Materials Society. pp. 234–252.

13. Mishra, R. S., and Ma, Z. Y. 2005. Review Article: Friction stir welding and processing. *Materials Science and Engineering R* 50: 1–78.

14. Wang, W., Shi, Q., Liu, P., Li, H., and Li, T. 2009. A novel way to produce bulk SiCp reinforced aluminum metal matrix composites by friction stir processing. *Journal of Materials Processing Technology* 209: 2099–3003.

15. El-Rayes, M. M., and El-Danaf, E. A. 2012. The influence of multi-pass friction stir processing on the microstructural and mechanical properties of aluminum Alloy 6082. *Journal of Materials Processing Technology* 212: 1157–1168.

16. Mazaheri, Y., Karimzadeh, F., and Enayati, M. H. 2011. A novel technique for development of A356/Al_2O_3 surface nanocomposite by friction stir processing. *Journal of Materials Processing Technology* 211: 1614–1619.

17. *Testing of metallic materials — Tension test*. 2009. German Institute for Standardization DIN 50125, Berlin, Germany.

18. *Material testing; Fatigue test, words, symbols, implementation, evaluation*. 1978. German Institute for Standardization DIN 50100, Berlin, Germany.

19. Dengel, D. 1975.The arcsin√P transformation — A simple method of graphical and computational evaluation of planned Wöhler fatigue tests. *Journal of Materials Engineering* 8: 253–288.

20. Massalski, T. B. 2001. *ASM Binary Alloy Phase Diagrams,* 2nd ed. Materials Park, Ohio: ASM International. pp. 31–46.

21. Davis, J. R. 1993. *ASM Specialty Handbook: Aluminum and Aluminum Alloys*. Materials Park, Ohio: ASM International.

22. Mondolfo, L. F. 1976. *Aluminum Alloys: Structure and Properties.* London, UK: Butterworths. pp. 173–175.

23. Ye, H. 2003. An overview of the development of Al-Si-alloy based material for engine applications. *Journal of Materials Engineering and Performance* 12: 288–297.

24. Raoa, D., Huber, K., Heerens, J., dos Santos, J. F., and Huber, N. 2013. Asymmetric mechanical properties and tensile behaviour prediction of aluminium alloy 5083 friction stir welding joints. *Materials Science and Engineering A* 565: 44–50.

25. Lee, W., Yeon, Y., and Jung, S. 2003. The joint properties of dissimilar formed Al alloys by friction stir welding according to the fixed location of materials. *Scripta Materialia* 49: 423–428.

26. Li, B., and Shen, Y. 2012. A feasibility research on friction stir welding of a new-typed lap-butt joint of dissimilar Al alloys. *Materials and Design* 34: 725–731.

27. Tutunchilar, S., Besharati Givi, M. K., Haghpanahi, M., and Asadi, P. 2012. Eutectic Al-Si piston alloy surface transformed to modified hypereutectic alloy via FSP. *Materials Science and Engineering A* 534: 557–567.

28. Asadi, P., Mahdavinejad, R. A., and Tutunchilar, S. 2011. Eutectic Al-Si piston alloy surface transformed to modified hypereutectic alloy via FSP simulation and experimental investigation of FSP of AZ91 magnesium alloy. *Materials Science and Engineering A* 528: 6469–6477.

29. Elangovan, K., and Balasubramanian, V. 2007. Influences of pin profile and rotational speed of the tool on the formation of friction stir processing zone in AA2219 aluminium alloy. *Materials Science and Engineering A* 459: 7–18.

30. Hong, S., and Suryanarayana, C. 2005. Mechanical properties and fracture behavior of an ultrafine-grained Al-20 wt pct Si alloy. *Metallurgical and Materials Transactions A* 36: 715–723.

31. Totten, G. E., and MacKenzie, D. S. 2003. *Handbook of Aluminum: Vol. 1: Physical Metallurgy and Processes*. New York, N.Y.: CRC Press. pp. 81–210.

32. Banerjee, S., and Ramanjan, R. V. 1996. *Advances in Physical Metallurgy*. New York, N.Y.: CRC Press. pp. 345–350.

33. Kung, C. Y., and Fine, M. E. 1979. Fatigue crack initiation and microcrack growth in 2024-T4 and 2124-T4 aluminum alloys. *Metallurgical and Materials Transactions A* 10: 603–609.

34. Shivkumar, S., Wang, L., and Apelian, D. 1991. Molten metal processing of advanced cast aluminum alloys. *JOM* 43: 26–32.

35. Sigler, D., Montpetit, M. C., and Haworth, W. L. 1983. Metallography of fatigue crack initiation in an overaged high strength aluminium alloy. *Metallurgical and Materials Transactions A* 14: 931–938.

36. Ren, S. R., Ma, Z. Y., and Chen, L. Q. 2008. Effect of initial butt surface on tensile properties and fracture behavior of friction stir welded Al-Zn-Mg-Cu alloy. *Materials Science and Engineering A* 479: 293–299.

37. Bisadia, H., Tavakolib, A., Tour Sangsarakia, M., and Tour Sangsaraki, K. 2013. The influences of rotational and welding speeds on microstructures and mechanical properties of friction stir welded Al5083 and commercially pure copper sheets lap joints. *Materials & Design* 43: 80–88.

38. Cerri, E., and Leo, P. 2010. Warm and room temperature deformation of friction stir welded thin aluminium sheets. *Materials & Design* 31: 1392–1402.